



Boron ignition and combustion with doped δ - Bi_2O_3 : Bond energy/oxygen vacancy relationships

Xizheng Wang^a, Tao Wu^a, Haiyang Wang^b, Jeffery B. DeLisio^a, Yong Yang^b, Michael R. Zachariah^{a,b,*}

^a Department of Chemistry and Biochemistry, University of Maryland, College Park, MD 20740, USA

^b Department of Chemical and Biomolecular Engineering, University of Maryland, College Park, MD 20740, USA

ARTICLE INFO

Article history:

Received 8 February 2018

Revised 2 May 2018

Accepted 18 July 2018

Available online 15 August 2018

Keywords:

Nanoenergetics

Thermite

Combustion

Boron

Bismuth oxide

ABSTRACT

The purpose of this paper is to extract a clearer relationship between atomic properties of the oxidizer, and ignition temperature and combustion kinetics. Pure Bi_2O_3 and a series of Y^{3+} and W^{6+} doped Bi_2O_3 nanoparticles with the same crystal structure and morphology were synthesized via aerosol spray pyrolysis and used as oxidizers in boron-based thermites. This enabled us to vary bond energy and oxygen vacancy concentration systematically. The ignition temperatures and the reactivities of different B/ Bi_2O_3 thermites were measured by rapid heating ($> 10^5$ K/s) temperature-jump/time-of-flight mass spectroscopy and a confined pressure cell, respectively. With pure Bi_2O_3 , the boron could be ignited at a temperature as low as 520 °C. In-situ high heating rate TEM was used to observe the reaction before/after heating. We find very clear relationships that higher oxygen vacancy concentration and smaller metal–oxygen bond energy lead to lower ignition temperature and higher combustion reactivity.

© 2018 Published by Elsevier Inc. on behalf of The Combustion Institute.

1. Introduction

Significant efforts have been devoted to the understanding and utilization of aluminum-based thermite systems, for pyrotechnics, propellants and explosives applications [1–6]. However boron is theoretically better due to its higher energy density [1]. Unlike aluminum, which has a low melting point of ~ 660 °C and a high melting point native oxide shell (~ 2072 °C), boron has a high melting point (~ 2076 °C) while its oxide, B_2O_3 , melts at a low temperature (~ 450 °C). In particular upon heating, molten B_2O_3 coats the solid boron core and inhibits the further oxidation of boron, which delays ignition and combustion [7,8], greatly limiting the performance of boron as a fuel. Studies on modifying the surface of boron particles to oxide-free and air-stable boron particles to improve ignition behavior have been investigated [9,10]. It is generally accepted that the combustion of micron sized boron particles occurs in two stages [11–13]: the first stage involves removal of the boron oxide shell, followed by a second stage of burning of the boron core. The transition from the first to the second stage requires the removal of boron oxide shell. Dreizin et al. studied the ignition of boron filaments in air and argon/oxygen mixtures and found that a phase change from α to β rhombohedral boron, triggered first stage ignition [14]. In recent years more efforts have

been devoted to the ignition and combustion of nano boron as the reduced length scale offers the potential to significantly reduce the energy release time and enhance the reactivity. Young et al. examined the ignition of nano boron and found a significantly shorter burn time compared with micron sized boron particles [15]. Sullivan et al. found that adding nano boron as a minor component in an Al/CuO thermite could enhance the thermite reactivity, but micro boron did not, and attributed this result to the fast melting of nano boron particles [8]. Other studies have primarily focused on macroscopic properties, i.e., particles size, crystallization of boron, etc. [11,16,17]. One issue however that has not been addressed, is what microscopic properties of the solid oxidizer are important to ignition and combustion performance when boron is employed as the fuel.

In a prior work using doped perovskites [18], where crystal structure and morphology were removed as variables, we found a clear correlation between the measured ignition temperature and atomic properties of the oxidizer, in particular, metal–oxygen bond energy, oxygen vacancy concentration, and electronegativity. However, perovskites have a relatively high metal–oxygen bond energy, which leads to a high ignition temperature and low combustion reactivity.

In a more recent work with aluminum as the fuel, we also found a correlation between oxygen ion conductivity in doped Bi_2O_3 and ignition temperature [19]. The oxygen ion conductivity of Bi_2O_3 is very sensitive to crystal structure, which is also highly

* Corresponding author.

E-mail address: mrz@umd.edu (M.R. Zachariah).

Table 1
Aerosol spray synthesized doped Bi₂O₃.

Doped Bi ₂ O ₃ formula	Abbreviation
(Y _{0.1} Bi _{0.9}) ₂ O ₃	YSB10
(Y _{0.15} Bi _{0.85}) ₂ O ₃	YSB15
(Y _{0.3} Bi _{0.7}) ₂ O ₃	YSB30
(Y _{0.4} Bi _{0.6}) ₂ O ₃	YSB40
(W _{0.05} Bi _{0.95}) ₂ O _{3,15}	WSB5
(W _{0.1} Bi _{0.9}) ₂ O _{3,3}	WSB10
(W _{0.15} Bi _{0.85}) ₂ O _{3,45}	WSB15
(W _{0.2} Bi _{0.8}) ₂ O _{3,6}	WSB20

temperature dependent: δ -Bi₂O₃ that has the highest conductivity is only stable between 730 °C, up to its melting point at 824 °C. Below 730 °C tetragonal β -Bi₂O₃ (at 650 °C) or the bcc γ -Bi₂O₃ (at 639 °C) is stable, and below about 500 °C the monoclinic α -Bi₂O₃ phase is most stable [20,21]. Among all the phases, cubic δ -Bi₂O₃ has the highest oxygen ion conductivity, which results from the large number of highly mobile oxygen vacancies, weak Bi–O bond and high polarizability of Bi³⁺ with its lone 6s² electrons [22]. In order to stabilize δ -Bi₂O₃ at room temperature, several studies have reported employing metal ion doping at bismuth sites [23,24]. In our recent study, 15% Er³⁺, Dy³⁺, Y³⁺, W⁶⁺ and Nb⁵⁺ were employed to stabilize δ -Bi₂O₃ [19]. Since δ -Bi₂O₃ has a defect fluorite-type crystal structure (AX₂), 25% of the oxygen sites in the unit cell are vacant [25,26], thus with Y³⁺ substitution which has the same valence as Bi³⁺, we expect the vacancy concentration to remain unchanged. However, W⁶⁺ has a higher oxidation state, so its substitution (i.e., WO₃) should correspondingly have ~50% more oxygen than AX₂ in the oxygen sites.

In this study we employ doped Bi₂O₃, synthesized via aerosol spray pyrolysis to enable systematic changes to the metal–oxygen bond energy, and oxygen concentrations. Key to this study is to make these changes while maintaining the same crystal structure, particle morphology and size. The ignition and combustion behavior were measured and analyzed by temperature-jump/time-of-flight mass spectrometry, and a constant-volume pressure cell. In-situ high heating rate transmission electron microscope was used to investigate the B/Bi₂O₃ reaction. Our results show that larger oxygen vacancy concentration and smaller metal–oxygen bond energy leads to lower ignition temperature, higher combustion reactivity with higher peak pressure, larger pressurization rate and shorter burn time.

2. Experimental

2.1. Materials

Boron particles (SB99, ~60 nm) were obtained from the SB Boron Corporation. Bi(NO₃)₃·5H₂O (≥98% pure) and Y(NO₃)₃·6H₂O (99.8% pure) were purchased from Sigma-Aldrich. (NH₄)₆W₁₂O₃₉·xH₂O was purchased from Alfa Aesar.

2.2. Synthesis of pure and doped Bi₂O₃

Doped Bi₂O₃ listed in Table 1 and Pure Bi₂O₃ were synthesized. All Bi₂O₃ particles were synthesized via aerosol spray pyrolysis [27,28] at 750 °C with a residence time of about 1 s from metal nitrate contained aqueous solutions formulated with the desired metal ratios. Nitric acid solution (2 mol/L) was used to dissolve Bi(NO₃)₃·5H₂O and deionized water was used to dissolve the other metal nitrates. For example, in order to synthesize (Y_{0.15}Bi_{0.85})₂O₃, a 0.2 mol/L precursor solution, containing stoichiometric Bi(NO₃)₃ and Y(NO₃)₃ was atomized by a nebulizer to generate nominally 1 μm droplets with compressed air. The atomized droplets passed

through a diffusion dryer, where most of the water was evaporated and then passed to a tubular furnace to produce the desired doped Bi₂O₃ particles. The final product was collected on a Millipore membrane with a pore size of 0.4 μm.

2.3. Synthesis of B/Bi₂O₃ thermites

Stoichiometric mixtures of SB99 boron particles and Bi₂O₃ were mixed and then sonicated in hexane for 30 min. While calculating the stoichiometry, the B₂O₃ shell (~30% of the mass) was considered. For the pressure cell test, thermites in hexane were dried in a hood overnight for hexane to evaporate.

2.4. Materials characterization

The crystal structures of the synthesized Bi₂O₃ were characterized by X-ray diffraction (XRD) performed on a Bruker D8 diffractometer with Cu K α radiation. Rietveld refinement of all diffraction patterns was performed with the TOPAS 4.2 software [29]. The morphologies of the Bi₂O₃ were measured by scanning electron microscopy (SEM) conducted on a Hitachi SU-70 instrument. Size distributions were obtained by measuring 300 individual nanoparticles statistically from SEM images of each sample, using Nano Measurer 1.2 image analysis software. The morphology of boron nano particles was measured by transmission electron microscope (TEM) with a JEM 2100 instrument and the elemental composition was measured by TEM equipped electron energy loss spectroscopy (EELS).

2.5. In-situ high heating rate TEM

The morphology changes of B/Bi₂O₃ were explored using Protochips rapid heating stages (Protochips, Inc.) within a TEM with a JEM 2100 instrument [30]. This stage provides rapid heating of the sample within the TEM, from room temperature to a maximum of 1200 °C, with tunable heating rate as high as 10⁶ °C/s. B/Bi₂O₃ sample was first heated to 480 °C at a rate of 4 × 10⁵ °C/s and then hold at constant temperature for 10 ms. TEM images were taken prior to and after rapid heating. The same procedures were repeated to heat the sample to 500, 520 and up to 825 °C in steps of ~20 °C and images were taken after each heating step. Elemental composition was measured by TEM equipped with energy dispersive X-ray spectroscopy (EDS).

2.6. Ignition temperature measurement of thermites

Ignition temperature was measured in a temperature-jump/time-of-flight mass spectrometer (T-jump/TOFMS) using direct optical emission with a high-speed camera (Vision Research Phantom v12.0) operating at 67,056 frames/s [31]. A hexane suspension of sample was coated onto a 70 μm diameter platinum filament, and allowed to air dry. The platinum wire can be joule heated at a rapid rate ~4 × 10⁵ °C/s, to ~1200 °C within 3 ms. The filament was directly inserted into the ionization region of a TOFMS, where the gaseous products could be temporally analyzed. The temperature of the wire was determined from electric resistance based on the Callendar–Van Dusen equation, through a simultaneous measure of temporal applied voltage and current. Due to the size of nanoparticles compared with the wire, and based on our previous result, the temperature of the wire is essentially equal to the temperature of the oxidizer system [32]. The ionization/extraction region of the TOFMS was pulsed at 10 kHz resulting in a full mass spectrum every 100 μs. A 600 MHz digital oscilloscope was used for data acquisition with a sampling rate of 100 megasamples/s.

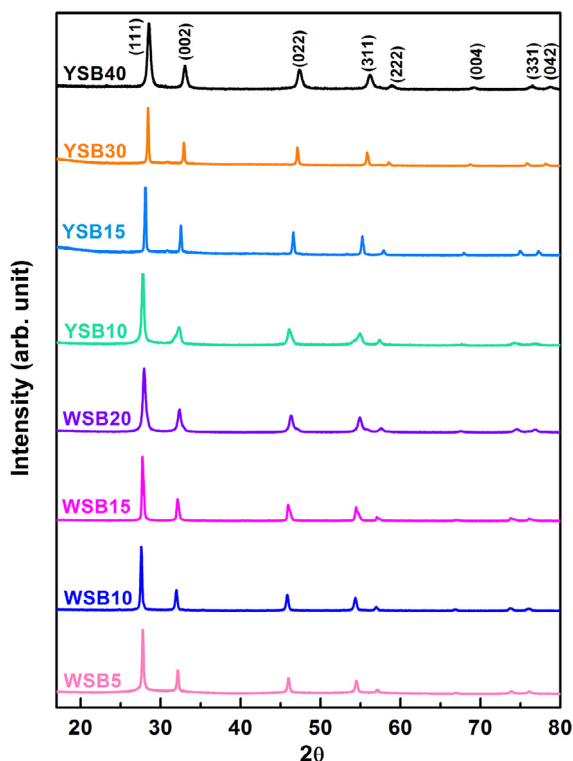


Fig. 1. X-ray diffraction patterns of aerosol spray synthesized doped Bi_2O_3 showing that all doped Bi_2O_3 have the same cubic phase in $Fm\bar{3}m$ space group.

2.7. Pressure cell measurement

Pressure and optical signal from thermite combustion were measured by a home-built pressure cell [33,34]. Briefly, a fixed mass of dry and loose thermite particles (25 mg) were placed on a small chip loaded into a fixed volume pressure cell (13 cm^3). A charged nichrome coil was used to ignite thermite by joule heating. Pressure was recorded by an attached piezoelectric pressure sensor, an in-line charge amplifier and signal conditioner. The optical signal was recorded simultaneously by a fiber optical sensor, containing a planoconvex lens ($f=50\text{ mm}$) and a high-speed photo detector.

3. Results and discussion

3.1. Structure and morphology

Figure 1 shows XRD patterns for YSB and WSB. Based on Rietveld refinements, all the synthesized doped Bi_2O_3 were $\delta\text{-Bi}_2\text{O}_3$ with a single cubic phase in $Fm\bar{3}m$ space group and the lattice parameters are listed in Table S1. This is important as we want to eliminate crystal structure as a potentially confounding variable in ignition and combustion behavior. Fig. S1 shows the XRD pattern of synthesized pure Bi_2O_3 , as $\beta\text{-Bi}_2\text{O}_3$ with a tetragonal structure.

Figure 2(a) and (b) shows SEM images of YSB30 and WSB20 as representative powders, indicating similar particle morphology and size distribution, consistent with our previous results [18,19]. Particle size distributions should be log-normally distributed corresponding to the original spray size distribution. Particle size distributions should be log-normally distributed corresponding to the original spray size distribution and are shown in Fig. 2(c) along with the log-normal fits of representative powders. The log-normal fit parameters are listed in Table S2, and indicate the synthesized doped Bi_2O_3 have similar narrow size distribution with $\sigma = 0.283 \pm 0.013$, and an average diameter of 90–100 nm. The

key point is that we can eliminate particle size and morphology as variables in ignition and combustion.

3.2. Ignition properties of B/undoped Bi_2O_3

3.2.1. T-Jump/TOFMS

T-Jump/TOFMS measurements were employed to study boron based thermite ignition at a heating rate of $\sim 4 \times 10^5\text{ }^\circ\text{C/s}$. Figure 3(a) shows the mass spectra of decomposition products of pure Bi_2O_3 , decomposed at $\sim 870\text{ }^\circ\text{C}$ (2.2 ms) with major peaks at m/z 209 (Bi^+), 104.5 (Bi^{2+}) and 32 (O_2^+). The peak at m/z 30 probably belongs to NO^+ , due to the incompletely decomposed nitrogen-containing impurities from the precursor and was common to all samples. When mixed stoichiometrically with boron, a violent reaction was initiated as seen in the frames from a high-speed camera as shown in Fig. 4. Based on the video, the ignition occurred at $\sim 520\text{ }^\circ\text{C}$ (0.892 ms) and the combustion event is short, $\sim 0.3\text{ ms}$ (from 0.892 ms to 1.190 ms). Figure 3(b) shows the corresponding B/ Bi_2O_3 mass spectra whose major products include m/z 43 (BO_2^+), 44 (HOBO^+), 70 (B_2O_3^+), 104.5 (Bi^{2+}) and 209 (Bi^+), minor products of 11 (B^+), 27 (BO^+), and again NO^+ impurities. B^+ and BO^+ and BO_2^+ may be occurring from electron impact fragmentation of B_2O_3^+ . To rule out the possibility that B_2O_3^+ was coming from the evaporation of the B_2O_3 shell, mass spectra of pure B are shown in Fig. S2 with no existence of any B-containing products listed above, indicating BO^+ , BO_2^+ , HOBO^+ and B_2O_3^+ are the products of reaction between B and Bi_2O_3 . From T-Jump/TOFMS we found no gaseous oxygen released prior to ignition, and thus conclude that the ignition of B/ Bi_2O_3 is a condensed phase reaction. Yeh and Kuo [17] reported the main ignition product of boron particles in gaseous oxygen include HOBO and BO_2 , while Ao et al. [35] reported the primary combustion product of boron contained propellant is B_2O_3 . These contradictions revealed that the combustion products were affected by many factors such as the ambient temperature, pressure, reaction atmosphere, and the physical and chemical properties of boron particles. Our results from T-Jump/TOFMS show that the main species released from B/ Bi_2O_3 were HOBO, B_2O_3 , BO_2 and BO, shown in Fig. 3.

Figure 5 shows the HOBO, B_2O_3 , BO and BO_2 release from B/ Bi_2O_3 , occurred within $\sim 0.3\text{ ms}$ (from $\sim 0.9\text{ ms}$ to 1.2 ms) and peaked between 1.0 and 1.1 ms and is consistent with the visual optical event time from the high speed camera (0.3 ms) with the maximum brightness at $\sim 1.05\text{ ms}$ shown in Fig. 4.

We were surprised by the low ignition temperature of B/ Bi_2O_3 ($\sim 520\text{ }^\circ\text{C}$), compared with the reported ignition temperatures of boron particles varying in the range of $1100\text{--}1700\text{ }^\circ\text{C}$ [36] and the ignition temperature of Al/ Bi_2O_3 ($\sim 630\text{ }^\circ\text{C}$ by Piekiet et al. [37]). TEM and EELS analysis of boron particles show that the boron nanoparticle has a B_2O_3 shell with a thickness of $\sim 2\text{ nm}$ (Fig. S3). As stated above, although boron has a high melting point core ($\sim 2076\text{ }^\circ\text{C}$), its oxide, B_2O_3 shell, melts at a low temperature ($\sim 450\text{ }^\circ\text{C}$). In addition, Bi_2O_3 also has a relatively low melting point ($\sim 817\text{ }^\circ\text{C}$) compared with other common metal oxides. We have already justified that the ignition of B/ Bi_2O_3 is a condensed phase reaction, dominated by solid-state diffusion [19]. Since the ignition temperature of B/ Bi_2O_3 is above the melting point of the B_2O_3 shell, suggests the possibility that molten B_2O_3 wetting Bi_2O_3 may play a role in ignition. To understand why B/ Bi_2O_3 ignites at such a low temperature, in-situ high heating rate TEM was employed to explore the morphology change of B/ Bi_2O_3 thermites.

3.2.2. In-situ TEM rapid heating

Figure 6(a) and (b) shows before and after heating images, and EDS for the thermite heated at $4 \times 10^5\text{ }^\circ\text{C/s}$ and held for 10 ms. Prior to heating, Fig. 6(a), shows (from EDS) that the dark

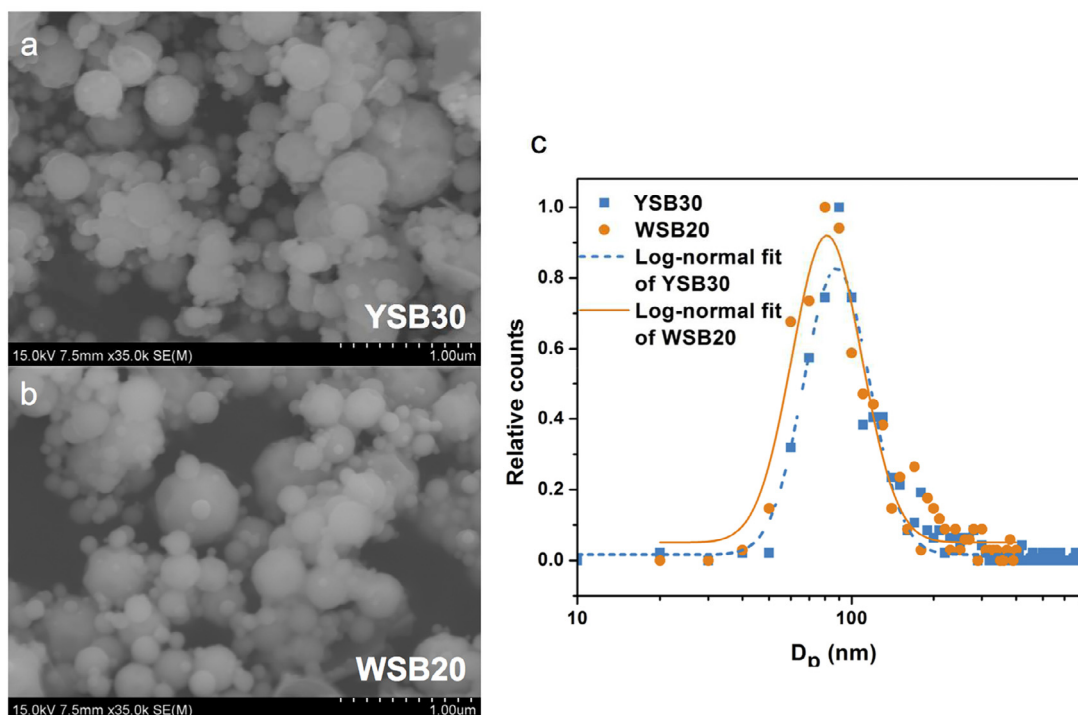


Fig. 2. SEM images of (a) YSB30 and (b) WSB20 particles; (c), particle size distributions and log-normal fit profiles of YSB30 and WSB20 with $\sigma = 0.283 \pm 0.013$.

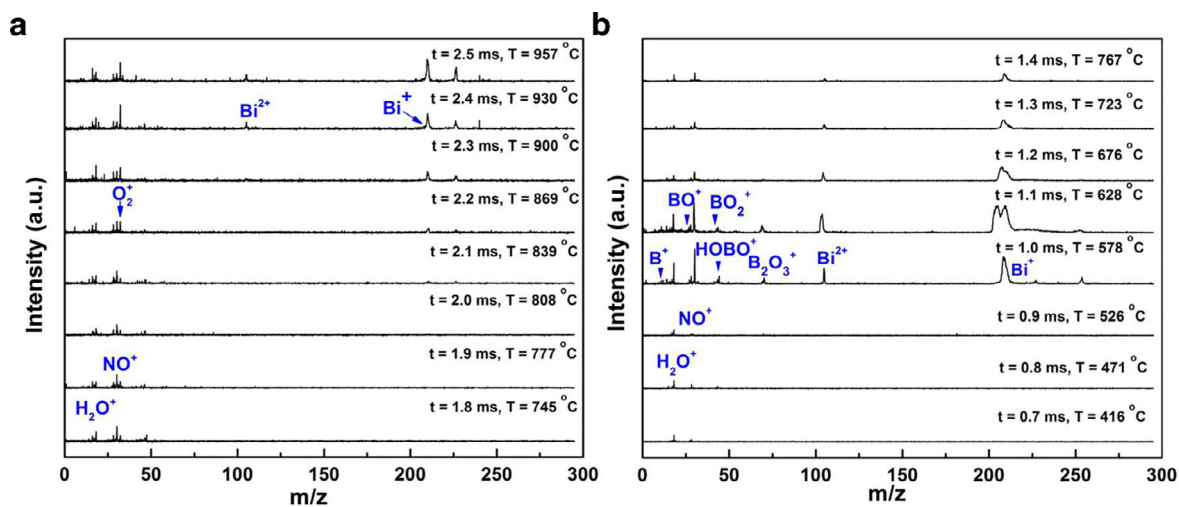


Fig. 3. Mass spectra for (a) Bi_2O_3 and (b) $\text{B}/\text{Bi}_2\text{O}_3$. Each spectrum is separated in time by $100 \mu\text{s}$.

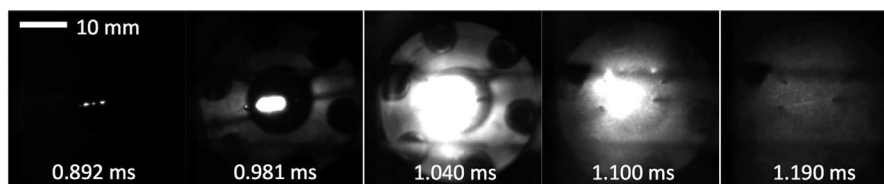


Fig. 4. High speed images of $\text{B}/\text{Bi}_2\text{O}_3$ during heating in T-Jump/TOFMS (scale bar applies for all images).

spherical particles are Bi_2O_3 while the light aggregates are boron. After rapid in-situ heating, we see in Fig. 6(b), that a large oval Bi particle was formed (indicated by the arrow). This is confirmed by the EDS line scan analysis across this particle which showed increased Bi but not O. With the boron core having a high melting temperature, the boron oxidation reaction must be strongly dependent on the diffusion of oxygen through the B_2O_3 shell. This can

be seen by comparing the dotted circled region in the inserts of Fig. 6(a) and (b). In Fig. 6(a), we observe that the interface between B and Bi_2O_3 is sharp. However, in the same area, after rapid heating, shown in the inset in Fig. 6(b), the region becomes highly diffuse without any discernable particle boundaries. We attribute this to the low melting points of B_2O_3 shell and Bi_2O_3 . The Tammann temperature ($T_{\text{Tammann}} = 0.5T_{\text{melting}}$) describes the temper-

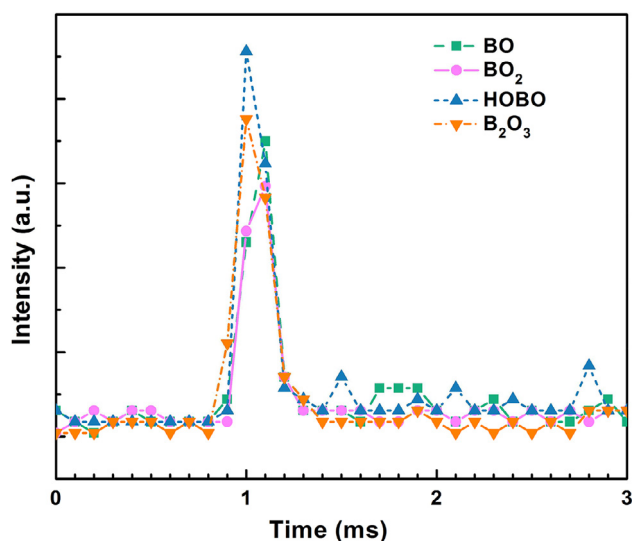


Fig. 5. BO, HOBO and B_2O_3 intensity released from B/ Bi_2O_3 T-Jump/MS.

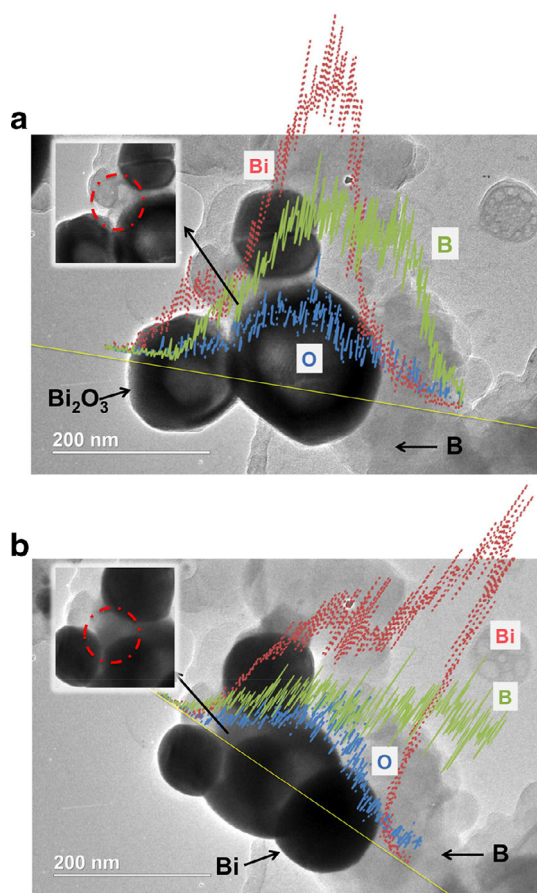


Fig. 6. TEM images and elemental line scan of (a) B/ Bi_2O_3 particles prior to in-situ heating. (b) Product of B/ Bi_2O_3 particles in panel (a) after in-situ heating at 4×10^5 °C/s to 825 °C for 10 ms (dot lines represent Bi, solid lines represent B and dash-dot lines represent oxygen).

ature, referenced to the melting point, at which atoms from the bulk exhibit appreciable mobility [38]. Given that the melting temperature of B_2O_3 is above the Tammann temperature of Bi_2O_3 , we propose that molten B_2O_3 wets Bi_2O_3 creating an interface so that high mobility condensed phase oxygen ions can diffuse through the liquid B_2O_3 shell. Comparing Fig. 6(a) and (b), we find reac-

Table 2

Metal–oxygen bond energy of doped Bi_2O_3 and calculated oxygen vacancy percentage in one unit cell and oxygen vacancy concentration, $[V_O]$, of doped Bi_2O_3 .

Thermite	M–O bond energy of oxidizer (kJ/mol)	Oxygen vacancy % of oxidizer	$[V_O]$ of oxidizer ($\#/cm^3$)
B + WSB5	158	21.3	9.7E21
B + WSB10	171	17.5	8.0E21
B + WSB15	184	13.8	6.4E21
B + WSB20	197	10	4.7E21
B + YSB10	159	25	1.2E22
B + YSB15	167	25	1.2E22
B + YSB30	189	25	1.2E22
B + YSB40	203	25	1.2E22

tion between B and Bi_2O_3 occurs only where they are physically in contact since there is no change observed for separated B or Bi_2O_3 particles. To better learn how the reaction was initiated, we stepwise increased the temperature in step of 10 or 20 °C from 480 °C to 825 °C to capture morphology changes.

A video generated by splicing individual TEM images of the thermite reaction can be found in the supplemental materials. It is obvious that throughout the whole heating process, boron particles were inert, without any obvious morphology changes due to its high melting point. With the limitation of resolution, we were not able to see the B_2O_3 shell. The volume of Bi_2O_3 particles increased as the temperature approached melting point (~ 817 °C) and eventually as seen in the last frame (825 °C), burst. Nevertheless reaction only occurred in the area where B and Bi_2O_3 were in contact. After heating to above 530 °C, some areas where B and Bi_2O_3 are in contact had obvious morphology changes and reaction is believed to occur with the formation of new particles (labeled in video). It is likely then that the low ignition temperature can be attributed to molten B_2O_3 wetting Bi_2O_3 creating access where high mobility solid-state oxygen can diffuse through the liquid B_2O_3 shell. This is in contrast to aluminum, where aluminum ions diffuse through a solid oxide shell, and thus requires that the core be somewhat mobile, which is why for almost all systems, the low temperature limit to aluminum ignition is near its melting point [4,19,39].

3.3. Ignition temperature: bond energy and oxygen vacancy considerations

Previous studies on aluminum-based thermites by our group employed a series of doped perovskites, and doped Bi_2O_3 with the aim of systematically varying metal–oxygen bond energy, and oxygen vacancy concentration [18,19]. In those studies we were able to see that the oxygen ion transport is a metric for thermite ignition and there exists a linear relationship, that lower metal–oxygen bond energies and larger oxygen vacancy concentrations lead to lower ignition temperature.

To see if the same behavior could be observed in another fuel, boron with seven doped bismuth oxides, which share the same crystal structure and particle morphology and size distribution, were mixed. Based on the lattice parameter and the fluorite structure of $\delta-Bi_2O_3$, the estimated oxygen vacancy ratio in the unit cell and oxygen vacancy concentrations are listed in Table 2. As discussed in our previous work, we calculated the metal–oxygen (M–O) bond energy of these synthesized doped Bi_2O_3 based on Eq. (1), where A stands for Bi, A' is the dopant metal and a is the dopant molar ratio. $\Delta(A-O)$ is calculated by Eq. (2), where $\Delta H_{A_mO_n}$ is the heat of formation of A_mO_n at 298 K, ΔH_A is the heat of sublimation of A-metal at 298 K and D_{O_2} is the dissociation energy of gaseous oxygen [40] and the calculated results are listed in Table 2.

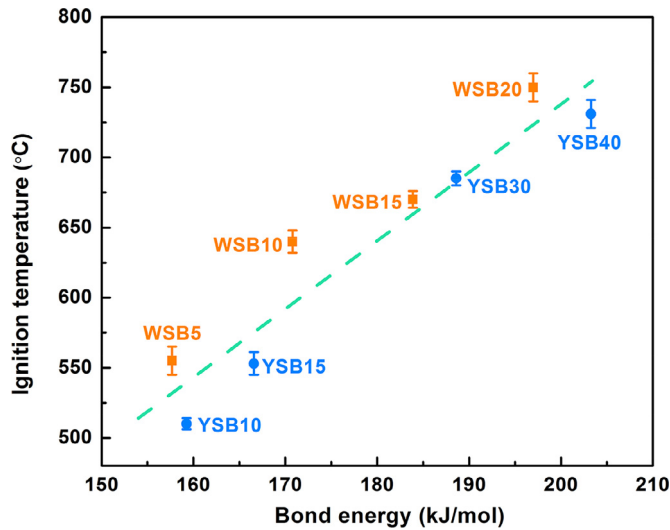


Fig. 7. Observed relationship between metal–oxygen bond energy of doped Bi_2O_3 versus the ignition temperatures of B/ Bi_2O_3 .

Thus doping with Y^{3+} or W^{6+} should increase bond energy. The higher the dopant ratio, the higher the metal–oxygen bond energy, and the more difficult should be oxygen ion migration.

$$M-O \text{ bond energy} = (1-a) \cdot \Delta(A-O) + a \cdot \Delta(A'-O) \quad (1)$$

$$\Delta(A-O) = \frac{1}{6m} \left(\Delta H_{A_m O_n} - m \Delta H_A - \frac{n}{2} D_{O_2} \right) \quad (2)$$

Figure 7 shows the relationship between our calculated metal–oxygen bond energy of doped Bi_2O_3 and the measured ignition temperature of B/doped Bi_2O_3 . There is a clear trend that M–O bond energy is proportional to the resultant ignition temperature. This is a gratifying result in that it is a second fuel confirming a result we previously observed with aluminum, and confirms that the likelihood that this is a general result [18,19]. Additionally, while bond energy dominates ignition temperature, exceptions were found, for example, YSB10 has higher metal–oxygen bond energy than WSB5 but has a lower ignition temperature. Presumably this is reflective of the importance of higher oxygen vacancy concentration. Thus we observe that smaller metal–oxygen bond energy and higher vacancy concentration lead to lower ignition temperature.

3.4. Combustion: bond energy and oxygen vacancy effects

We can divide the synthesized doped Bi_2O_3 into two groups: YSB with constant 25% oxygen vacancy in the lattice and WSB with varying oxygen vacancy ratio. Pressure cell measurements of those two groups of doped Bi_2O_3 with boron were taken so as to study the effects of oxidizers' bond energy and oxygen vacancy for boron based thermite combustion properties. According to previous studies [33], the optical intensity generally correlates with the flame temperature in the pressure cell. Peak pressure, pressurization rate obtained from the pressure signal and burn time obtained by measuring the peak's full width at half maximum are three parameters that we use to evaluate the combustion performance of thermites. Pressure histories of B with doped Bi_2O_3 can be found in Fig. S4. Figure 8(a) shows the pressurization rate for B/doped Bi_2O_3 thermite versus the metal–oxygen bond energy of oxidizer. We find that the pressurization rate and peak pressure of thermite reaction decreased significantly with increased metal–oxygen bond energy of oxidizer. Pressurization rate dropped one order of magnitude from WSB5 to WSB20 and three orders from YSB15 to YSB40. It is generally acknowledged that gaseous products contribute to the pressure rise [28,41], in which low-boiling point Bi (1564 °C) makes it an important gaseous species that increases pressure in the thermite reaction since both Y (3338 °C) and W (5555 °C) have high boiling point. Thus with more W^{6+} or Y^{3+} doped in Bi_2O_3 , less gaseous Bi is produced and thus peak pressure is further lowered. It is also noted that although YSB10 and YSB15 have higher bond energy and lower Bi molar ratio than WSB5, they showed significantly higher pressurization rates than B/WSB5, which is probably due to the higher oxygen vacancy concentrations. Thus both metal–oxygen bond energy and oxygen vacancy concentration in oxidizer affect the combustion performance of B/doped Bi_2O_3 thermites. Since the pressurization rate can be correlated with the flame propagation velocities, or reactivity, one would assume that a system with a larger pressurization rate would show a shorter burn time. Thus the burn time is expected to show a reversed trend as pressurization rate with the bond energy of oxidizer. Figure 8(b) shows the burn time for B/doped Bi_2O_3 thermite versus the metal–oxygen bond energy of oxidizer and indicate that burn time generally increased with the metal–oxygen bond energy of doped Bi_2O_3 as expected.

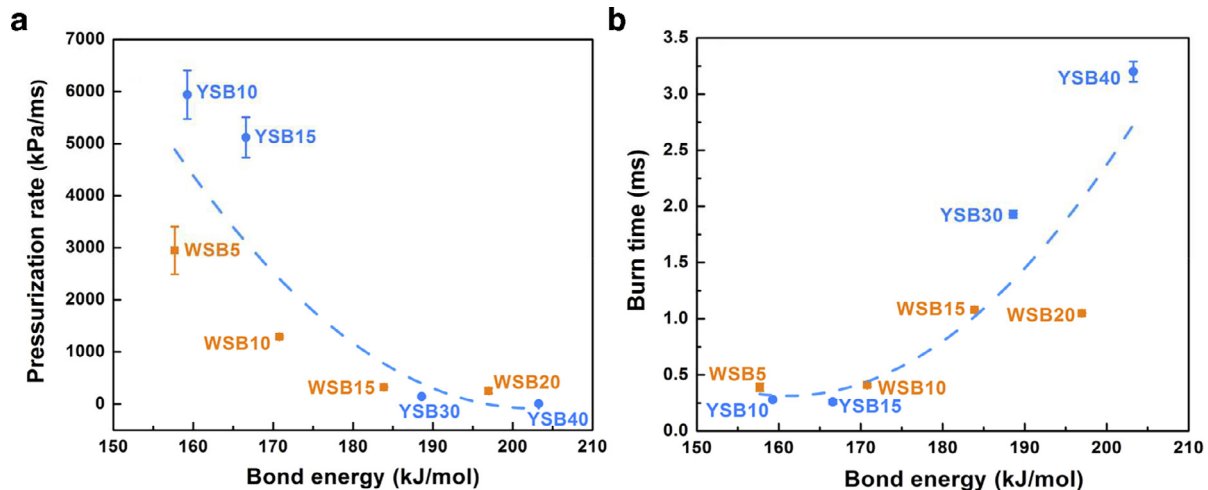


Fig. 8. Pressurization rate (a) and burn time (b) of B/doped Bi_2O_3 thermite versus metal–oxygen bond energy of doped Bi_2O_3 .

4. Conclusions

In summary, our study reveals a clear relationship between molecular properties of the oxidizer and ignition temperature as well as combustion performance (pressure peak, pressurization rate and burn time) of boron based nano-thermites. This was enabled by employing a systematically doped Bi_2O_3 , whose crystal structure and particle size and morphology are maintained the same, but whose oxygen vacancy concentration and bond energy are varied. We found a clear relationship that larger oxygen vacancy concentration and smaller metal–oxygen bond energy lead to lower ignition temperature and higher combustion reactivity with higher peak pressure, pressurization rate and shorter burn time of boron based thermites. In addition, in-situ high heating rate TEM was used to explore the morphology change, both prior to and after the initiation of $\text{B/Bi}_2\text{O}_3$. We proposed that $\text{B/Bi}_2\text{O}_3$ ignites (~ 520 °C) at lower temperature than $\text{Al/Bi}_2\text{O}_3$ (~ 630 °C) because, and in part based on TEM images, the molten B_2O_3 wets Bi_2O_3 creating an interface so that high mobility solid-state oxygen can diffuse through the liquid B_2O_3 shell.

Acknowledgments

This work was supported by the Army Research Office. Special thanks to Dr. Sz-Chian Liou and Dr. Wen-An Chiou for technical assistance.

Supplementary materials

Supplementary material associated with this article can be found, in the online version, at doi:10.1016/j.combustflame.2018.07.015.

References

- [1] E.L. Dreizin, Metal-based reactive nanomaterials, *Prog. Energy Combust. Sci.* 35 (2009) 141–167.
- [2] W. Zhou, J.B. DeLisio, X. Wang, M.R. Zachariah, Reaction mechanisms of potassium oxysalts based energetic composites, *Combust. Flame* 177 (2017) 1–9.
- [3] J.J. Granier, M.L. Pantoya, Laser ignition of nanocomposite thermites, *Combust. Flame* 138 (2004) 373–383.
- [4] W. Zhou, J.B. DeLisio, X. Wang, G.C. Egan, M.R. Zachariah, Evaluating free vs bound oxygen on ignition of nano-aluminum based energetics leads to a critical reaction rate criterion, *J. Appl. Phys.* 118 (2015) 114303.
- [5] H. Wang, R.J. Jacob, J.B. DeLisio, M.R. Zachariah, Assembly and encapsulation of aluminum NP's within AP/NC matrix and their reactive properties, *Combust. Flame* 180 (2017) 175–183.
- [6] N. Eisenreich, H. Fietzek, M. del Mar Juez-Lorenzo, V. Kolarik, A. Koleczko, V. Weiser, On the mechanism of low temperature oxidation for aluminum particles down to the nano-scale, *Propellants Explos. Pyrotech.* 29 (2004) 137–145.
- [7] B. Van Devener, J.P.L. Perez, J. Jankovich, S.L. Anderson, Oxide-free, catalyst-coated, fuel-soluble, air-stable boron nanopowder as combined combustion catalyst and high energy density fuel, *Energy Fuels* 23 (2009) 6111–6120.
- [8] K. Sullivan, G. Young, M.R. Zachariah, Enhanced reactivity of nano-B/Al/CuO MIC's, *Combust. Flame* 156 (2009) 302–309.
- [9] K.L. Chintersingh, M. Schoenitz, E.L. Dreizin, Oxidation kinetics and combustion of boron particles with modified surface, *Combust. Flame* 173 (2016) 288–295.
- [10] J.F. Xi, J.Z. Liu, H.P. Li, Y. Wang, Y.W. Zhang, J.H. Zhou, K.F. Cen, Progress in methods of promoting the ignition and combustion of boron particles, *Han-neng Cailiao/Chin. J. Energ. Mater.* 21 (2013) 533–538.
- [11] A. Mačević, J.M.K. Semple, Combustion of boron particles at atmospheric pressure, *Combust. Sci. Technol.* 1 (1969) 181–191.
- [12] A. Ulas, K.K. Kuo, C. Gotzmer, Ignition and combustion of boron particles in fluorine-containing environments, *Combust. Flame* 127 (2001) 1935–1957.
- [13] A.P. Il'in, G.V. Yablunovskii, A.A. Gromov, E.M. Popenko, N.V. Bychin, Combustion of mixtures of ultrafine powders of aluminum and boron in air, *Combust. Explos. Shock Waves* 35 (1999) 656–659.
- [14] E.L. Dreizin, D.G. Keil, W. Felder, E.P. Vicenzi, Phase changes in boron ignition and combustion, *Combust. Flame* 119 (1999) 272–290.
- [15] G. Young, K. Sullivan, M.R. Zachariah, K. Yu, Combustion characteristics of boron nanoparticles, *Combust. Flame* 156 (2009) 322–333.
- [16] G. Mohan, F.A. Williams, Ignition and combustion of boron in O_2 /inert atmospheres, *AIAA J.* 10 (1972) 776–783.
- [17] C.L. Yeh, K.K. Kuo, Ignition and combustion of boron particles, *Prog. Energy Combust. Sci.* 22 (1996) 511–541.
- [18] X. Wang, T. Wu, M.R. Zachariah, Doped perovskites to evaluate the relationship between fuel-oxidizer thermite ignition and bond energy, electronegativity and oxygen vacancy, *J. Phys. Chem. C* 121 (2017) 147–152.
- [19] X. Wang, W. Zhou, J. DeLisio, G. Egan, M.R. Zachariah, Doped δ -bismuth oxides to investigate oxygen ion transport as a metric for condensed phase thermite ignition, *Phys. Chem. Chem. Phys.* 19 (2017) 12749–12758.
- [20] H.A. Harwig, On the structure of bismuthsesquioxide: the α , β , γ , and δ -phase, *Z. Anorg. Allg. Chem.* 444 (1978) 151–166.
- [21] D.W. Jung, K. Duncan, E.D. Wachsman, Doubly doped Bi_2O_3 electrolytes with higher conductivity, *ECS Trans.* 1 (2006) 63–71.
- [22] T. Takahashi, H. Iwahara, High oxide ion conduction in sintered oxides of the system Bi_2O_3 - WO_3 , *J. Appl. Electrochem.* 3 (1973) 65–72.
- [23] E.D. Wachsman, S. Boyapati, N. Jiang, Effect of dopant polarizability on oxygen sublattice order in phase-stabilized cubic bismuth oxides, *Ionics* 7 (2001) 1–6.
- [24] M.J. Verkerk, A.J. Burggraaf, High oxygen ion conduction in sintered oxides of the Bi_2O_3 - Dy_2O_3 system, *J. Appl. Electrochem.* 128 (1981) 75–82.
- [25] X. Wang, R. Jayatilake, D.D. Taylor, E.E. Rodriguez, M.R. Zachariah, Study of C/doped δ - Bi_2O_3 redox reactions by in operando synchrotron X-ray diffraction: bond energy/oxygen vacancy and reaction kinetics relationships, *J. Phys. Chem. C* 122 (2018) 8796–8803.
- [26] K.Z. Fung, H.D. Baek, A.V. Virkar, Thermodynamic and kinetic considerations for Bi_2O_3 -based electrolytes, *Solid State Ionics* 52 (1992) 199–211.
- [27] T. Wu, A. SyBing, X. Wang, M.R. Zachariah, Aerosol synthesis of phase pure iodine/iodic biocide microparticles, *J. Mater. Res.* 32 (2017) 890–896.
- [28] G. Jian, L. Liu, M.R. Zachariah, Facile aerosol route to hollow CuO spheres and its superior performance as an oxidizer in nanoenergetic gas generators, *Adv. Funct. Mater.* 23 (2013) 1341–1346.
- [29] R.W. Cheary, A.A. Coelho, Fundamental parameters approach to X-ray line-profile fitting, *J. Appl. Crystallogr.* 25 (1992) 109–121.
- [30] J.B. DeLisio, X. Wang, T. Wu, G.C. Egan, R.J. Jacob, M.R. Zachariah, Investigating the oxidation mechanism of tantalum nanoparticles at high heating rates, *J. Appl. Phys.* 122 (2017) 245901.
- [31] L. Zhou, N. Piekielek, S. Chowdhury, M.R. Zachariah, T-Jump/time-of-flight mass spectrometry for time-resolved analysis of energetic materials, *Rapid Commun. Mass Spectrom.* 23 (2009) 194–202.
- [32] S. Chowdhury, K. Sullivan, N. Piekielek, L. Zhou, M.R. Zachariah, Diffusive vs explosive reaction at the nanoscale, *J. Phys. Chem. C* 114 (2010) 9191–9195.
- [33] K. Sullivan, M.R. Zachariah, Simultaneous pressure and optical measurements of nanoaluminum thermites: investigating the reaction mechanism, *J. Propul. Power* 26 (2010) 467–472.
- [34] H. Wang, G. Jian, W. Zhou, J.B. DeLisio, V.T. Lee, M.R. Zachariah, Metal iodate-based energetic composites and their combustion and biocidal performance, *ACS Appl. Mater. Interfaces* 7 (2015) 17363–17370.
- [35] W. Ao, Y. Wang, S. Wu, Ignition kinetics of boron in primary combustion products of propellant based on its unique characteristics, *Acta Astronaut.* 136 (2017) 450–458.
- [36] D. Sundaram, V. Yang, R.A. Yetter, Metal-based nanoenergetic materials: synthesis, properties, and applications, *Prog. Energy Combust. Sci.* 61 (2017) 293–365.
- [37] N.W. Piekielek, L. Zhou, K.T. Sullivan, S. Chowdhury, G.C. Egan, M.R. Zachariah, Initiation and reaction in $\text{Al/Bi}_2\text{O}_3$ nanothermites: evidence for the predominance of condensed phase chemistry, *Combust. Sci. Technol.* 186 (2014) 1209–1224.
- [38] J.A. Moulijn, A.E. Van Diepen, F. Kapteijn, J.A. Moulijn, A.E. Van Diepen, F. Kapteijn, Catalyst deactivation: is it predictable? What to do? *Appl. Catal. A* 212 (2001) 3–16.
- [39] T. Wu, X. Wang, P.Y. Zavalij, J.B. DeLisio, H. Wang, M.R. Zachariah, Performance of iodine oxides/iodic acids as oxidizers in thermite systems, *Combust. Flame* 191 (2018) 335–342.
- [40] D.R. Lide, Standard thermodynamic properties of chemical substances, *CRC Handbook of Chemistry and Physics*, 2007.
- [41] G. Jian, J. Feng, R.J. Jacob, G.C. Egan, M.R. Zachariah, Super-reactive nanoenergetic gas generators based on periodate salts, *Angew. Chem. Int. Ed.* 52 (2013) 9743–9746.